ADVANCED ENERGY & SUSTAINABILITY RESEARCH
Open Access
www.advenergysustres.com

A Model for Modulating Oxide Ion Transport with Endo-Particles for Application in Energy Conversion

*Stephen James Dalton and Dragos Neagu**

Certain energy conversion processes are underpinned by the transport of oxide ions across materials, components, or interfaces. Examples include solid oxide fuel cells not only for power generation from hydrogen, but also chemical looping for hydrogen and syngas generation. Identifying new ways of enhancing oxide ion transport is thus required for advancing such technologies. Traditionally, this is achieved by doping or crystal lattice engineering but recent reports in these fields suggest a new approach, where oxide ion transport is potentially modulated through embedded (endo-) nanoparticles. This is assumed to occur due to the strain that endo-particles induce throughout the material. Here, a model is proposed to rationalize this effect, by constructing corresponding visual and numerical models of these experimental systems and calculating their respective volumetric strain and resulting conductivity enhancement. The proposed model indicates a strong correlation between ion conductivity enhancement and observed experimental data in these two different applications. This result demonstrates how nanoparticles may be harnessed within materials, to modulate oxide ion transport properties, beyond their traditional role as catalytic centers, which could inspire the design of new nanostructured oxide ion conductors for energy conversion applications.

1. Introduction

Oxide ion transport in oxides is instrumental for enabling various energy conversion technologies including, but not limited to solid oxide fuel cells and electrolyzers, oxygen separation membranes, and chemical looping.[1–5] For example, in solid oxide cells (**Figure 1**a), oxide ion conduction is required not only in the electrolyte, which ensures the selective transport of oxide ions between electrodes, preventing the reactants from mixing directly, but also within the electrodes responsible for electrochemically breaking down the reactants into respective ions and transporting them to the electrolyte.[2,4] In chemical looping (Figure 1b), an oxygen carrier material reversibly exchanges oxygens, by reacting successively with a reducing stream (e.g., CH_4), during which oxide ions are supplied to form the products (e.g., syngas), and then an oxidizing stream (e.g., O_2), where the oxide ions are replenished (cations also undergo redox changes to preserve charge neutrality).[5,6]

Oxide ion transport is typically controlled and enhanced by chemical substitution, doping, or crystal lattice engineering. Notable examples include yttria-substituted zirconia (YSZ), the "classic" ion conductor, magnesium-doped lanthanum strontium gallates (LSGM), a perovskite ion conductor with a relatively high conductivity at intermediate temperatures, and also more recently ferroelectric and hexagonal perovskite oxide structures.[4,7–10] A more exotic form of ion transport modulation is through strain, the artificial distortion of a crystal lattice.[11–17] Tensile strain, for example, involves "stretching" the crystal lattice, which seemingly allows more space for ion transport and lowers the activation energy for ion migration.[11,13] Generally, strain is induced by depositing the material of interest as a thin film upon a substrate, which results in a mismatch in lattice parameters between the two crystalline phases (ε_i), causing an artificial expansion or contraction of the thin-film layer.[12,13,15] Elastic relaxation, and potentially the formation of interfacial dislocations, then confines strain and its effects to a small region near the interface, which extends to no more than 100 nm.[12,13,18] Therefore, strain effects are generally limited to thin films and the nanoscale.

However, two recent studies from the fields of solid oxide cells (SOC) and chemical looping (CL) suggest that strain might be induced in macroscopic systems by dispersing nanoparticles within the oxide ion conductor matrix, i.e., as internal or "endo-particles" (Figure 1c). This would effectively introduce a dense distribution of spherical interfaces, thus propagating the interface misfit ε_i throughout the volume. The SOC study prepared such a system by assembling and sintering gold (Au) nanoparticles with a double perovskite oxide matrix $Pr_{1.9}Ni_{0.71}Cu_{0.41}Ga_{0.05}O_{4+\delta}$ (PNCO) and measured up to ≈2.5-fold increase in ion conductivity for an Au to PNCO matrix content of 1–3 mol%.[19] The CL study employed exsolution from a perovskite $La_{0.8}Ce_{0.1}Ni_{0.4}Ti_{0.6}O_3$ to form nickel oxide (NiO) nanoparticles within a residual perovskite

S. J. Dalton, D. Neagu
Department of Chemical and Process Engineering
University of Strathclyde
G1 1XJ, UK
E-mail: dragos.neagu@strath.ac.uk

The ORCID identification number(s) for the author(s) of this article can be found under https://doi.org/10.1002/aesr.202200054.

DOI: 10.1002/aesr.202200054

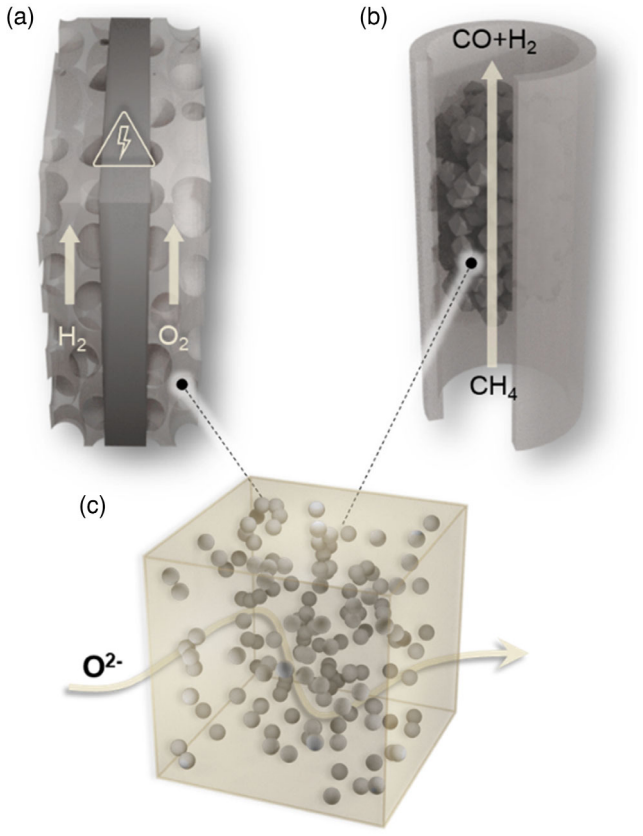

Figure 1. Current applications of endo-particle systems. Schematic illustrations of: a) solid oxide fuel cells for power generation from hydrogen, b) chemical looping for methane conversion to syngas. c) Endo-particle systems.

titanate matrix, (La,Ce)(Ti,Ni)O_3 (LTNO). They observed a ≈2–9-fold increase in oxygen exchange for a NiO to LTNO content of ≈5–25 mol%.[6] In exsolution, chosen species (e.g., Ni) are initially incorporated on the B-site of an A-site-deficient $A_{1-x}BO_3$ perovskite host lattice, and, through a redox treatment, is forced to precipitate from these sites as nanosized particles.[20,21] While both results remain intriguing and potentially technologically important, there is currently no model that describes how strain might correlate with conductivity enhancement in these new endo-particle systems and thus how the effect might be rationalized and used to guide future material design.

Here we develop a model that describes the spatial configuration of endo-particles within materials, and calculates the degree of strain throughout the volume, based on the interface misfit parameter, particle size and separation, particle to matrix loading, as well as various other material properties. Our model can reasonably account for the observed particle content and conductivity enhancement correlations and reveal that indeed volumetric strain can serve as a suitable descriptor for oxide ion conductivity enhancement in endo-particle systems. We also discuss certain discrepancies owing to the complexity of the systems and suggest possible solutions to address them in future studies.

2. Results and Discussion

2.1. Spatial Configuration of the Endo-Particle Systems

We approach modeling by first constructing the equivalent 3D representation of the systems. This serves to define not only their respective spatial configurations but is also a basis for calculating average strain throughout the material volume, as shown in the next subsection. For this, we define a volume element of arbitrary size within the material, which we term a voxel, as a basis for calculations. For the purpose of visualizing particle spatial configurations, we employ a voxel with an edge of 100 nm, but for calculations voxels with edges of 500 nm are used to ensure the results are representative at a macroscopic scale. We then populate this voxel with nanoparticles of size and number derived from the structural information available in the original studies. Note that their location is randomized, but their size and number are calculated based on the particle to matrix content (mol%) mentioned in the original studies.

For the SOC systems, formed by sintering and henceforth labeled with "S", we define "S1", "S2" and "S3" as corresponding to the systems with 2, 5, and 7 nm particle sizes, respectively, according to the original study.[19] For the CL systems, formed by exsolution and henceforth labeled with "E", we define "E1", "E2", and "E3" as corresponding to the systems with 4, 7, and 12 nm particle sizes described in the original study.[6] The 100 nm edge voxels corresponding to systems S1–S3 and E1–E3 can be seen in **Figure 2**a,b, respectively. Figure 2c shows their particle count per voxel, which is representative of particle concentration per unit volume, one of the parameters that is expected to dictate the average level of strain within the material. It is apparent from this figure that the particle population in the S sample varies over a greater range, ≈30 to ≈400 per voxel, as compared to the E sample which varies between ≈50 and ≈200 particles per voxel. Visually and qualitatively, the endo-particles in sample E appear to "fill" the voxel volume to a larger degree compared to sample S (owing to a higher particle/matrix mol% content in the E sample) and thus we anticipate a greater degree of volumetric strain in samples E.

The corresponding inter-particle distance is plotted in Figure 2d. The values represent the average distance between neighboring particles (at their surface), since these are the regions where strain is being imposed by the particles onto the host matrix. The distances were obtained by calculating the Euclidian distances between each individual particle within the voxels to its neighbors and averaging out the distance values across the entire particle set within the respective voxel (500 nm edge voxels). The results in Figure 2d indicate that, consistent with particle populations, the inter-particle distance varies over a greater range for the S sample, between ≈20 and ≈40 nm, and over a much tighter range for the E sample, between ≈15 and ≈20 nm. This is important since, as mentioned in the introduction, strain decays rapidly with distance, and therefore the E sample with its narrower inter-particle distance is expected to ensure more homogenous strain coverage throughout the material volume. It should be noted that while there is no experimental data available for the average inter-particle distance for sample S, such data is available for sample E, from large area cross-section microscopy data in the original study

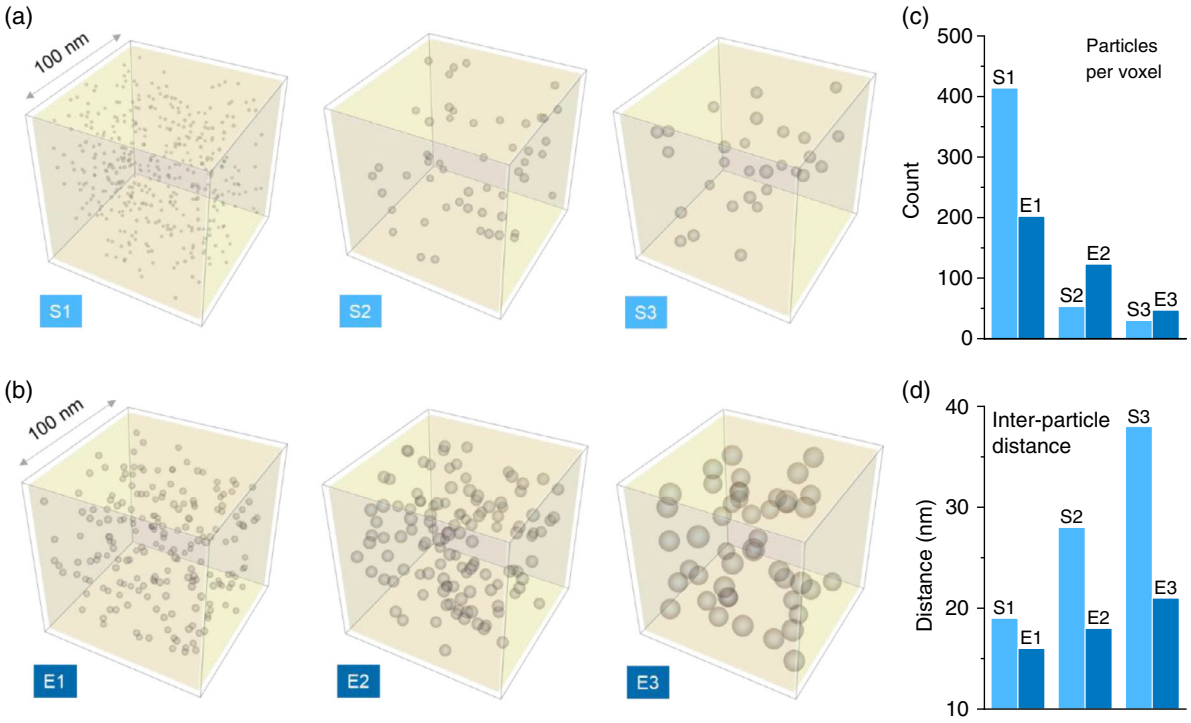

Figure 2. Visualization and spatial configuration of endo-particle systems. a) Calculated voxels of 100 nm edge corresponding to systems S1–S3. b) Calculated voxels of 100 nm edge corresponding to systems E1–E3. c,d) Plots of: c) the particle count per voxel and d) inter-particle distance, corresponding to the systems S and E shown in (a) and (b), respectively.

(see Supporting Information and Methods in ref. [6] for the microscopy data and analysis methodology, respectively). The average experimental inter-particle distances reported, as center-to-center particle distance, for E1, E2, and E3, were 20, 25, and 32 nm, respectively, which, when factoring in particle diameter matches our calculated average inter-particle values. This validates our approach to modeling the spatial configuration of endo-particle systems in a way that is consistent with available experimental data and shows that this method can be used to characterize these systems visually and quantitatively.

2.2. Modeling Local Strain in Endo-Particle Systems

To the best of our knowledge, to date, there has been no attempt to calculate strain within a macroscopic volume where the strain foci are particles, as is the case here (**Figure 3**a). In fact, as

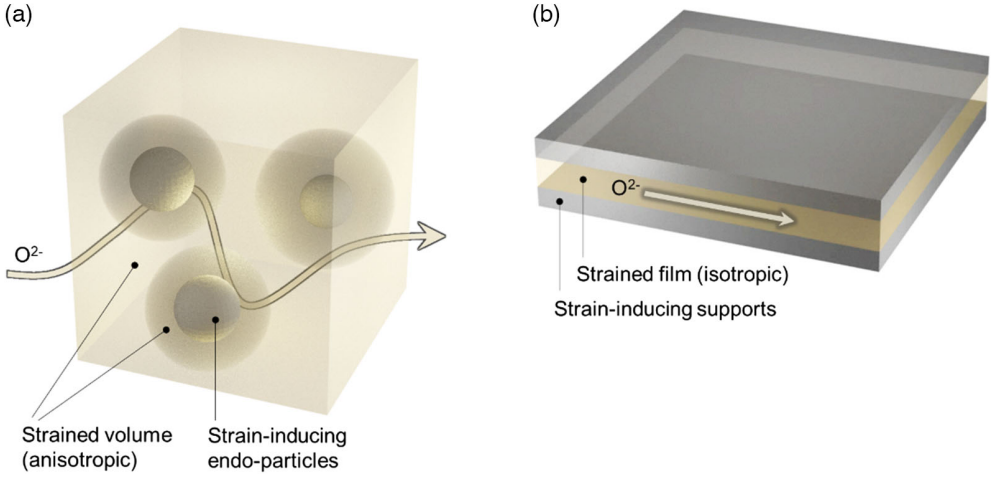

Figure 3. Strain and ion transport in different geometries. Schematic representation of strain and conduction in: a) endo-particle system and b) thin-film system.

highlighted in the introduction, strain is generally only realized in thin films where the strained phase and the strain-inducing phase are both planar (Figure 3b). To address this challenge, while still building upon the conceptual advances in modeling strain in planar systems, we draw a parallel between the endo-particle and planar systems. For a planar system, the strain experienced by a film strained in tandem by two adjacent layers (see Figure 3b), can be readily calculated through a model developed by Korte et al. (see **Figure 4**a).[12] By analogy, in the endo-particle systems, the tandem layers correspond to pairs of particles operating in tandem to strain a discrete region of the material volume. The average strain throughout the material volume could thus be considered to arise from the combined contribution of each particle working as a strain tandem pair with all its neighbors, computed for each and every particle within a voxel.

To this end, we adapt the model developed by Korte et al., which quantifies strain in thin film multilayer electrolyte systems.[12] Figure 4a provides a visual depiction of the tandem interactions which we utilize to describe strain between pairs of particles. The particles induce lattice mismatch with the surrounding matrix at the interface; this results in an interfacial misfit strain, ε_i, which is calculated from the crystal lattice parameters of the particle and matrix, a_p and a_m respectively.

$$\varepsilon_i = \frac{a_p - a_m}{a_m} \tag{1}$$

Since a coherent interface is formed (experimentally confirmed for the E systems, in particular, see ref. [6]), we assume this to be entirely elastic. The dimension of the strained matrix zone is denoted by d (inter-particle distance), and the length of the interface by l. The term δ is the distance from the interface at which the elastic energy of the system is minimized and mathematically characterises the rate at which strain decays. Based on previous reports,[12,18] the parameter δ can be expressed as a function of only the interface length, l, and the Poisson's ratio of the surrounding matrix, ν.

$$\delta = \left(\frac{1}{4}\sqrt{\frac{2}{3}\frac{1-\nu}{1+\nu}}\right) l \tag{2}$$

Under the aforementioned assumptions, the length of the interface l corresponds to half the particle circumference since this is the length over which two particles straining the matrix in a tandem pair would be facing each other. Considering the axes origin at the midpoint between the strain-inducing interfaces, it follows that elastic strain in the x direction, ε_{xx}, is equivalent to that in the y direction, ε_{yy}, such that $\varepsilon_{xx} = \varepsilon_{yy} = \varepsilon$ for all values of z.[18] The elastic strain ε at any position z, $\varepsilon(z)$, follows an exponential decay type function, reaching maximum strain ε_i at $z = -d/2$ and $d/2$, which corresponds to the two strain-inducing interfaces. It follows that local strain, $\varepsilon_L(z)$, can be expressed as a hyperbolic function.

$$\varepsilon_{xx} = \varepsilon_{yy} = \varepsilon(z) = \frac{\varepsilon_i}{1 + e^{-d/\delta}}\left(e^{\frac{z-d/2}{\delta}} + e^{-\frac{z+d/2}{\delta}}\right) \tag{3}$$

$$\varepsilon_L(z) = \varepsilon_i \frac{\cosh z/\delta}{\cosh \frac{d}{2\delta}} \tag{4}$$

This relation describes the elastic strain profile between two interfaces and thus between two particles separated by

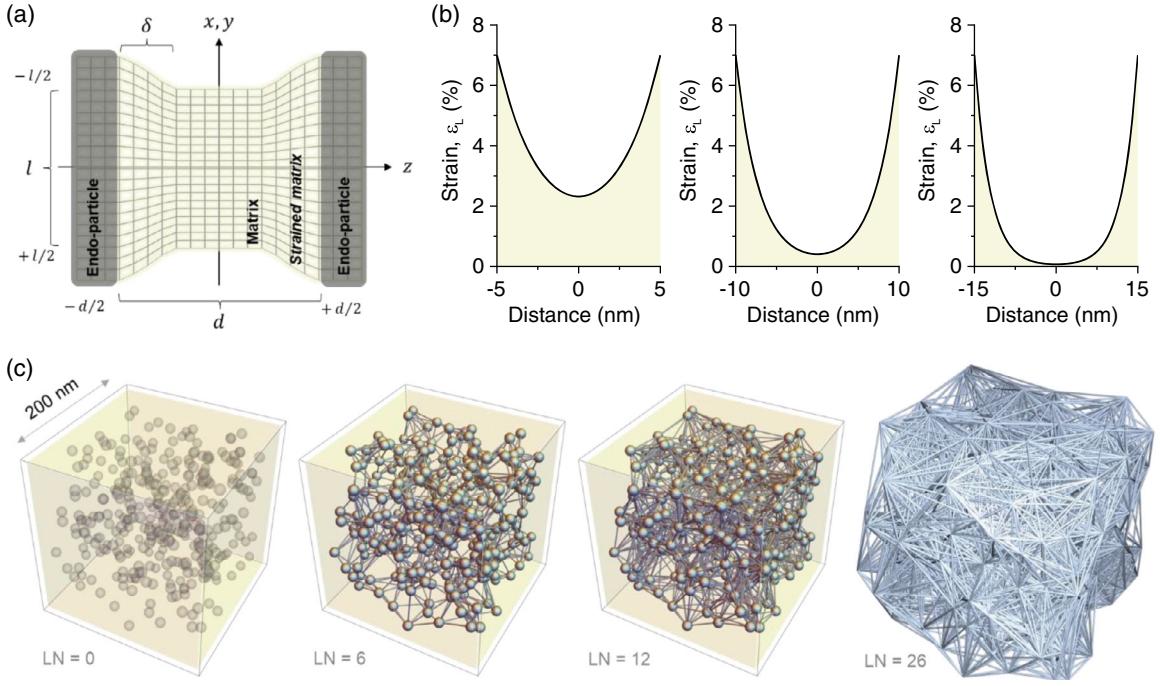

Figure 4. Modeling local and volumetric strain in endo-particle systems. a) Local strain induced in a host matrix in between the surfaces of a tandem pair of endo-particles. b) Plots of local strain between pairs of particles at different inter-particle distances. c) A voxel of 200 nm edge corresponding to system E3, and showing from left to right the endo-particles, and connecting lines to the closest 6, 12, and 26 local neighbors (voxel and particles not shown in the latter).

distance d. To illustrate the strain profiles that may be observed for the endo-particle systems, we exemplify the results of this equation for system E3, in Figure 4b. For the E systems, ε_i has a value of 0.07, or 7%, as calculated from Equation (1) on the basis of a NiO–LTNO interface with the lattice parameter of the perovskite obtained from the original study.[6] An interface strain value of 7% is generally considered to be relatively high, and in this instance, some strain would be expected to be relieved through the formation of dislocations. However, experimental reports of NiO thin films on $SrTiO_3$ show that this is not the case, and thus an $\varepsilon_i = 7\%$ is feasible and is used in the calculations in this study.[22] Moreover, for endo-particle systems, the area of contact between the strain-inducing phase (nanoparticle) and the strained phase (perovskite matrix) is much smaller than in a thin film and therefore elastic strain would be more easily accommodated. For ν, we use a value of 0.3, which is representative of these systems. Detailed explanation regarding the calculation of material parameters used in this study, based on corroborated data from the literature and the Materials Project open-web database, is given in Note S1, Supporting Information.[23–29] We then plot the strain profiles over three different inter-particle distances, 10, 20, and 30 nm, as shown in Figure 4b. We do so, even though the average inter-particle distance in this system is ≈20 nm, because in reality particles will interact with neighboring particles over a variety of distances, shorter or longer than the average value, as discussed in the next section. This provides a more representative view of the range of strain profiles that may be encountered throughout the volume and thus the plots in Figure 4b illustrate that strain in endo-particle systems is considerably more anisotropic than in a thin-film system. Figure 4b also shows that strain decays rapidly with increasing inter-particle distance, as mentioned in the introduction also. In this system, strain decreases to less than 1/10 of its maximum value over a distance of ≈8 nm. This illustrates the importance of maintaining a homogenous and short inter-particle distance for achieving higher coverage of volumetric strain in the endo-particle systems.

2.3. From Local to Volumetric Strain

As hypothesized at the beginning of Section 2.2, volumetric strain, defined as the average strain throughout the material volume, could be calculated from the combined strain contribution of each particle and its subset of neighboring tandem pairs, computed for each particle within a representative-size voxel. It is, therefore, important to consider the number of neighbors that constitute this subset. For example, in an ideal cubic symmetry system with k spacing, for each particle, there are 6 near-neighbors at k distance (cube edges), 12 next-near-neighbors at $k\sqrt{2}$ distance (cube face diagonals), and 8 next-next-near-neighbors at $k\sqrt{3}$ distance (cube diagonal). There are thus 26 local neighbors (henceforth referred to as LN) in the proximity of each particle. This number appears to be representative of experimental systems also. For example, the cross-section microscopy data for sample E in the original study reveal an in-plane LN of ≈6–8 from Voronoi tessellation analysis.[6] Considering three orthogonal planes, a spatial LN of ≈18–24 seems sensible.

To illustrate the impact that different LN values have in probing strain coverage within the volume, we exemplify this for sample E, on a voxel size of 200 nm. An exemplification for sample S is shown in Figure S1, Supporting Information, for comparison. Figure 4c shows the voxel with its constituting particles, followed by voxels where the coordination to neighboring particles is represented by lines, for LN = 6, 12, and 26. This analysis illustrates that when the LN is increased, a greater volume fraction of the voxel is being filled or probed for strain and therefore LN = 26 would be most representative of the average strain throughout the volume. Additionally, this illustrates yet again the inherent anisotropy of strain in the endo-particle systems, and the need to probe the entirety of the volume to ensure the calculated volumetric strain is also representative of a percolation volume since ion transport in this case is volumetric rather than 2D as it is in the case of thin films (see Section 2.4 for further discussion on the importance of percolation for conduction also).

To calculate volumetric strain, we thus consider a representative-size voxel (e.g., 500 nm). Within this voxel, we first calculate the average strain between each particle and its 26 LNs. The local strain for each tandem pair, $\overline{\varepsilon_L}$, can be calculated by integrating Equation (4) over the distance corresponding to each LN, d_{LN}

$$\overline{\varepsilon_L} = \frac{2}{d_{LN}} \int_0^{d_{LN}/2} \varepsilon_i \frac{\cosh z/\delta}{\cosh \frac{d_{LN}}{2\delta}} dz \tag{5}$$

Average volumetric strain, $\overline{\varepsilon_V}$, is then the average value of strain computed for each particle interaction with its subset of LN = 26 LNs, for all n particles within a voxel.

$$\overline{\varepsilon_V} = \frac{1}{n} \sum_1^n \left(\frac{1}{LN} \sum_1^{LN} \overline{\varepsilon_L} \right) \tag{6}$$

The calculated average volumetric strain values $\overline{\varepsilon_V}$ for the series S and E are plotted in **Figure 5**. The ε_i and ν values for systems E are the same as used in Section 2.2. For the S systems, $\varepsilon_i = 3.9\%$, which corresponds to the relevant Au/PNCO interfaces according to the original study, and $\nu = 0.3$ (see Note S1, Supporting Information, for calculation of material parameters). Figure 5a shows that the strain values for samples S1–S3 range between ≈0.2% and 0.6%, respectively, while for samples E1–E3, between ≈0.9% and 2.2%, respectively. No experimental information on volumetric strain was provided in the original study for sample E which would have allowed us to verify the validity of our calculations for these systems. However, such information is available for sample S where approximate volumetric strain values were calculated from X-Ray data, which is in fact a volume averaging technique.[19] The values reported for samples S1–S3 were in the range of 0.3–0.55% which are in very good agreement with our calculated values, indicating that our approach to volumetric strain modeling is representative of strain values that may be observed experimentally. The slight discrepancy between the calculated and experimental range of strain values is likely to be due to particle size inhomogeneity in these samples, inherent to their mixing and sintering preparation method (see Section 2.5 also).

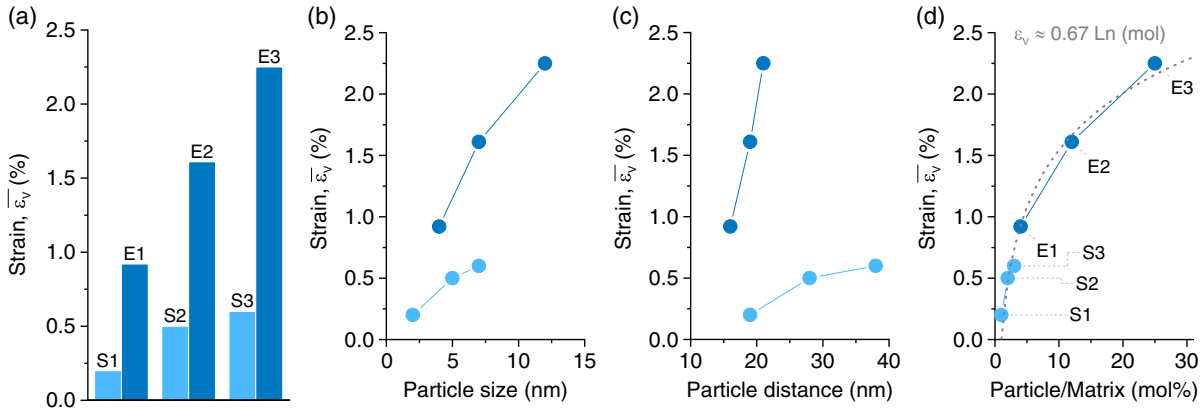

Figure 5. Volumetric strain in endo-particle systems. a) volumetric strain calculated for systems S and E. b–d) Volumetric strain as a function of: b) particle size, c) average inter-particle distance, d) mol% of particles with respect to the host matrix. Errors are of the size of points used for plotting and lines serve as a guide to the eye.

To identify the parameters with which $\overline{\varepsilon_V}$ correlates, we plot against particle size, inter-particle distance, and particle/matrix mol% content, in Figure 5b–d, respectively. Figure 5b shows that generally strain increases with increasing particle size, but at different rates for systems S and E. For systems E, strain increases more rapidly with increasing particle size, while the increase in strain with increasing size in system S appears to be more incremental. A similar trend, but in a more dramatic contrast is seen in Figure 5c, which shows that strain increases very rapidly with increasing inter-particle distance for E systems, but increases slowly and reaches a plateau for sample S. This is counter-intuitive since strain should decrease with increasing distance (see Figure S2, Supporting Information). In part this is due to the particle/matrix mol% content increasing in parallel, but also by the fact that inter-particle distance varies in a much tighter range for sample E, ≈15–20 nm, as compared to sample S, ≈20–40 nm (Figure 2d). This indicates that size and inter-particle distance are not independent descriptors for volumetric strain. By plotting volumetric strain as a function of particle/matrix mol% content, all the samples appear to fall into a more meaningful trend. The correlation between volumetric strain and the particle/matrix mol content seems to follow a logarithmic function, whereby $\varepsilon_V(\%) \approx 0.67\text{Ln}(\text{mol}\%)$. This reveals mol content as a useful descriptor for volumetric strain since it naturally combines both size and inter-particle distance, presumably as long as the nanoparticles remain at the nanoscale size. Therefore, for endo-(nano)particle systems, it is ultimately the nanoparticle loading, in conjunction with interfacial strain ε_i, and, to a lower extent, host matrix mechanical parameters such as ν, that dictate the achievable volumetric strain.

Based on the aforementioned analysis, for the purpose of guiding future material design, one might conclude that increasing the overall particle phase fraction will lead to increasingly higher benefits in terms of strain. The gain rate appears to follow a log scale dependency, as shown in Figure 5d, and is conditional on maintaining particle size and inter-particle distance at the nanoscale range homogenously throughout the volume, as in the case of E systems. The upper limit to which increasing particle phase fractions may be possible, and therefore the "optimum" levels, might be dictated by the change in mechanical properties of the matrix following the incorporation of metal particles. For example, a ceramic containing embedded nanoparticles beyond a certain mol fraction may become too brittle to be used in practice. In the case of E systems, 25 mol% was feasible, but there is no report of an upper limit in this system. This indicates that experimental and theoretical mechanical property analysis may be essential in the design of endo-particles systems for future applications.

2.4. From Volumetric Strain to Ionic Conductivity Enhancement

According to previous studies, strain can be linked to ionic conductivity via internal pressure.[12,29] A pressure profile between interfaces, $p(z)$, can be expressed as a function of the elastic strain profile. This involves consideration of the stress tensor in the system and the application of generalized Hooke's law. The mathematical derivation is included in Note S2, Supporting Information, and the resulting expression is as follows.

$$p(z) = -\frac{2}{3}\frac{Y}{(1-\nu)}\varepsilon_i \frac{\cosh z/\delta}{\cosh \frac{d}{2\delta}} = -\frac{2}{3}\frac{Y}{(1-\nu)}\varepsilon_L(z) \tag{7}$$

where Y and ν are Young's modulus and Poisson's ratio of the material, respectively. In our model, we have utilized data in the literature to account for Y and ν variation with temperature (see Note S1, Supporting Information). Equation (7) thus links internal pressure to local strain between tandem particle pairs.

Importantly, a thermodynamic relation between isotropic pressure and the space available for defect migration (activation volume) can be derived and expressed mathematically through transition state theory and the Nernst–Einstein diffusion equation.[12,29] The resultant expression is as follows.

$$\ln\frac{\sigma_\varepsilon(z)}{\sigma_0} = -\frac{\Delta V_m}{RT}p(z) \tag{8}$$

where the σ_ε is the conductivity under strain, σ_0 is the conductivity of the unstrained material, occurring at $p(z) = 0$, and thus $\sigma_\varepsilon/\sigma_0$ is the ionic conductivity enhancement under strain.

Therefore, $\ln\frac{\sigma_\varepsilon(z)}{\sigma_0}$ is the natural logarithm of the conductivity enhancement at a position z, and ΔV_m is the migration (activation) volume of the defect migration process which encapsulates the degree to which pressure affects conduction.

By substituting Equation (7) in (8), we arrive at the following expression where parameter α is dimensionless and conveniently contains all material constants.

$$\ln\frac{\sigma_\varepsilon(z)}{\sigma_0} = \alpha\varepsilon_L(z) \quad \text{with} \quad \alpha = \frac{2}{3}\frac{\Delta V_m Y}{RT(1-\nu)} \tag{9}$$

The average local conductivity enhancement, $\overline{\sigma_{\varepsilon,L}}/\sigma_0$, can be calculated as an integral average of the local conductivity $\sigma_\varepsilon(z)$, within the limits $z = \{-d_{LN}/2, d_{LN}/2\}$.

$$\frac{\overline{\sigma_{\varepsilon,L}}}{\sigma_0} = \frac{1}{d_{LN}}\int_{-d_{LN}/2}^{d_{LN}/2} e^{\alpha\varepsilon_L(z)}\mathrm{d}z = \frac{2}{d_{LN}}\int_0^{d_{LN}/2} e^{\alpha\varepsilon_L(z)}\mathrm{d}z \tag{10}$$

If we approximate the function $\varepsilon_L(z)$ with its corresponding average value, $\overline{\varepsilon_L}$ over the respective integration range $\{-d_{LN}/2, d_{LN}/2\}$, calculated according to Equation (5), this allows the further simplification of Equation (10).

$$\frac{\overline{\sigma_{\varepsilon,L}}}{\sigma_0} \approx e^{\alpha\overline{\varepsilon_L}} \tag{11}$$

In essence, Equation (11) illustrates how the average conductivity scales with average strain in two dimensions, i.e., between a particle and a neighbor. By analogy, it seems reasonable to assume that a similar dependency will scale to three dimensions. That is, the average volumetric conductivity enhancement, $\overline{\sigma_{\varepsilon,V}}/\sigma_0$, is expected to vary as a function of average volumetric strain, $\overline{\varepsilon_V}$, in a manner analogous to Equation (11).

$$\frac{\overline{\sigma_{\varepsilon,V}}}{\sigma_0} \approx e^{\alpha\overline{\varepsilon_V}} \tag{12}$$

It is important to note that incorporating strain into our expression for ionic conduction in this manner somewhat accounts for the phenomena of ionic transport percolation. As ions pass through the 3D structure formed by neighboring endo-particles, they are expected to travel "fastest" when in close proximity to nanoparticle surfaces (where strain is higher), and subsequently "slow" in the low-strained matrix between particles (Figure 3a). Ion transport is thus not isotropic in an endo-particle system, unlike thin-film systems where ions may travel in close proximity to an interface and effectively form 2D, isotropic, ion transport highways throughout the material (Figure 3b). Therefore, considering the multitude of tandem pair interactions, as described in Section 2.3, contained within parameter $\overline{\varepsilon_V}$ implicitly addresses this concept. Equation (12), therefore, expresses the ionic conduction enhancement of the material as a function of the degree of strain in three dimensions.

2.5. Strain-Conductivity Model Validation Against Experimental Data

To validate our strain-conductivity model expressed through Equation (12), we apply it to the conductivity data available in the original studies of the S and E systems. For this, we employ the $\overline{\varepsilon_V}$ values calculated in Section 2.3. For calculating the α parameter, ν, Y, ΔV_m, and T need to be defined for the respective systems. For the temperature, T, the experimental values were used, i.e., 873 and 800 K, for systems S and E, respectively.[6,19] To calculate the material parameters, we corroborated the literature data with data available from the open-web access Materials Project database, as detailed in Note S1, Supporting Information.[23–30] For both systems, at the operating temperature range, $\nu = 0.3$, and $Y = 140$ GPa. For the migration volume, ΔV_m, a value of 4.6 $cm^3\,mol^{-1}$ was calculated for the E systems, and a value of 7.5 $cm^3\,mol^{-1}$ for the S systems.

For the S systems, the authors report oxygen self-diffusion coefficients for samples S1–S3, and also for the unstrained, reference samples. We normalize the reported oxygen diffusion coefficients values by that of the unstrained system to produce a dimensionless number representative of the diffusion enhancement factor, which can then be compared with our own average volumetric conductivity enhancement, $\overline{\sigma_{\varepsilon,V}}/\sigma_0$. The comparative results of our model and the experimental results are shown in **Figure 6**a. This comparison shows that for samples S1 and S2 there is a good agreement between our model and the experimental oxide ion diffusion enhancement, suggesting our approach to modeling the strain-conductivity relationship detailed in Section 2.4 is experimentally relevant. However, upon reaching sample S3, there is a sharp drop in conductivity enhancement, even below the unstrained, reference value. It is possible that this may be in part due to the method in which oxygen diffusion was measured, based on ^{18}O labeling profiles, which could be prone to measurement errors if the samples are not well-enough densified, which could be expected as the Au particle content increases from samples S2 to S3. However, strain (calculated here, but also measured experimentally as explained in Section 2.3) does not seem to increase at the same rate when going from samples S2 to S3, as compared with samples S1–S2 (see Figure 5a,d). This potentially suggests inhomogeneity issues with respect to particle size (agglomeration) which, again could occur during the mixing and sintering of the phases and which could leave large areas of the volume unstrained. Our model shows that when particle size increases, mimicking agglomeration, the volumetric strain also decreases (see Figure S2, Supporting Information). Nonetheless, it is worth noting that the relatively modest maximum volumetric strain achieved of ≈0.5% was sufficient to increase oxygen transport by a factor of ≈2, which in turn led to a significant increase in SOC cell power density by a factor of ≈2.5.[19]

For system E, the authors report oxygen exchange time constants which may serve as a reasonable basis of comparison, although they are also susceptible to measurement errors. The study reports oxygen exchange time constant values for samples E1–E3, but also for the unstrained phase. Similarly, we normalize the reported oxygen exchange time constants by that of the unstrained system to produce a dimensionless number representative of the oxygen transport enhancement factor, which can then be compared with our own average volumetric conductivity enhancement, $\overline{\sigma_{\varepsilon,V}}/\sigma_0$. The comparative results of our model and the experimental results are shown in Figure 6b. This comparison shows that there is a good agreement between our model and

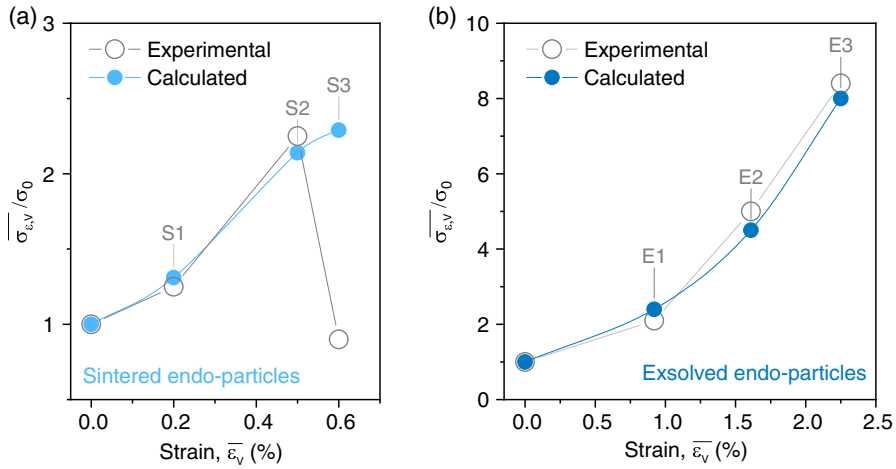

Figure 6. Strain-conductivity model validation against experimental data. a,b) Average conductivity enhancement comparing experimental and calculated values as a function of average volumetric strain for: a) S system and b) E system. Experimental values for ion conductivity enhancement were calculated from the original studies, for systems S[19] and E.[6] Errors are of the size of the points used for plotting; lines serve as a guide to the eye.

the experimental data across the entire data set, from samples E1–E3, indicating that overall this system behaves much closer to a model system as compared to system S. This is perhaps not surprising considering the much narrower inter-particle distance variation range observed for this system, as compared to the S systems, as shown in Figure 2d. For the samples with larger particle loading and thus higher degrees of strain, E2 and E3, the calculated conductivity increase is slightly lower than the experimental value. This potentially indicates that at such high particle concentration levels other effects, besides strain, for example, interfacial point defects, may also contribute to increasing conductivity, as observed recently.[31,32] Another aspect to note is that this plot shows that the maximum oxide ion conductivity enhancement factor of ≈8.5 observed experimentally in this system is accounted for by a volumetric strain of ≈2.2%. The magnitude of this strain value may appear to be relatively large, however, it is consistent with other literature values observed for thin-film perovskites, where 2–2.5% strain can increase conductivity several folds up to an order of magnitude, at temperatures similar to the current study.[17,29] This illustrates that the exsolution method for the preparation of endo-particle systems is suitable for producing systems with relatively large volumetric strain and thus relatively large conductivity enhancement. Finally, it is worth noting, from an application perspective, the relatively high strain of ≈1.6–2.2% led to an increase in oxygen transport by a factor of ≈5-8.5, which contributed, among other factors, to lowering methane to syngas chemical looping conversion from 900 to 600 °C, and a selectivity increase from ≈80 to 98%.[6]

3. Conclusions

In this study, we formulated a theoretical basis for rationalizing the modulating effect that nanoparticles exhibit on oxide ion transport, when embedded within oxide matrices, in a so-called endo-particle system. We apply our model to two previously reported systems, one prepared by the assembly (co-sintering) for application in solid oxide fuel cells for power generation from hydrogen, and the other one prepared by exsolution (endogenesis) for methane conversion to syngas by chemical looping. We proposed a method for visualizing and calculating the spatial configuration of endo-particles, as well as the resulting volumetric strain and ion conductivity enhancement that endo-particles induce in the host matrix. Our results show that volumetric strain scales with respect to the amount of endo-particles (as mol content vs host matrix) in a seemingly logarithmic function. From a practical point of view, this can be visualized as 2–7 nm endo-particles, with an inter-particle distance of 15–40 nm, totaling ≈1–3 mol%, led to ≈0.2–0.5% volumetric strain and conductivity enhancement by a factor of 1.2–2.3, and endo-particles with 4–12 nm, and inter-particle distance of 15–20 nm, totaling ≈5–25 mol% led to ≈0.9–2.2% volumetric strain and a conductivity enhancement factor from ≈2.1 to 8.5. Both sets of enhancements had a substantial impact on their respective technologies.

Overall, our proposed strain-conductivity model accounts reasonably well for the observed experimental data, validating our approach, although some discrepancies still remain. This is in part due to the insufficient number of data sets available in the literature, but also in part due to the model's reliance on accurate structural and conductivity experimental data, as well as various material mechanical property data. Some of these parameters may be readily available in the literature, while others may not. Additionally, a greater variety and range of endo-particle systems would have to be experimentally and theoretically investigated to take this intriguing new concept forward. Based on the exciting potential of the endo-particle systems that our study revealed and rationalized, we believe that this will soon inspire new nanostructured materials capable of a generational leap in terms of ion conductivity for energy conversion applications.

4. Experimental Section

The computations were coded and carried out using the software Wolfram Mathematica 13. The code is available from the authors upon reasonable request.

The number of particles was calculated as

$$n = \frac{f \times \vartheta \times M_p}{\rho_p \times \frac{4}{3}\pi \times \left(\frac{s}{2}\right)^3} \quad (13)$$

where n is the number of particles, f is the mol fraction of particle phase with respect to the matrix phase, ϑ is the mols of matrix phase considered, s is the particle diameter, and M_p and ρ_p are the molar mass and density of the particle phase, respectively.

The edge of a voxel was calculated as

$$\text{voxel} = \sqrt[3]{\vartheta \times a_m^3 \times N_A + \frac{f \times \vartheta \times M_p}{\rho_p}} \quad (14)$$

where a_m is the cell parameter of the matrix phase and N_A. is Avogadro's constant.

Any subsequent calculations relating to the methodology are detailed in the main text of the paper. Material parameter data calculation is detailed in Note S1, Supporting Information.

Supporting Information

Supporting Information is available from the Wiley Online Library or from the author.

Acknowledgements

D.N. gratefully acknowledges the Royal Society for the grant RGS/R1/211253 and The Royal Society of Edinburgh for the grant Scotland-Germany hydrogen Research Scheme, "DiTo-H2 A digital toolbox for hydrogen production".

Conflict of Interest

Part of the results are submitted towards an invention disclosure and potential invention patent with the University of Strathclyde.

Data Availability Statement

The data that support the findings of this study are available from the corresponding author upon reasonable request.

Keywords

chemical looping, endo-particles, energy conversions, fuel cells, oxide ion transports, perovskites, strains

Received: April 12, 2022
Revised: September 2, 2022
Published online:

[1] R. A. De Souza, in *Resistive Switching* (Eds.: D. Ielmini, R. Waser), Wiley-VCH Verlag GmbH & Co. KGaA, Weinheim, Germany **2016**, pp. 125–164.
[2] B. C. H. Steele, A. Heinzel, *Nature* **2001**, *414*, 345.
[3] S. P. S. Badwal, F. T. Ciacchi, *Adv. Mater.* **2001**, *13*, 993.
[4] L. Malavasi, C. A. J. Fisher, M. S. Islam, *Chem. Soc. Rev.* **2010**, *39*, 4370.
[5] A. Thursfield, A. Murugan, R. Franca, I. S. Metcalfe, *Energy Environ. Sci.* **2012**, *5*, 7421.
[6] K. Kousi, D. Neagu, L. Bekris, E. I. Papaioannou, I. S. Metcalfe, *Angew. Chem. Int. Ed.* **2020**, *59*, 2510.
[7] T. Ishihara, H. Matsuda, Y. Takita, *J. Am. Chem. Soc.* **1994**, *116*, 3801.
[8] M. Li, M. J. Pietrowski, R. A. De Souza, H. Zhang, I. M. Reaney, S. N. Cook, J. A. Kilner, D. C. Sinclair, *Nat. Mater.* **2014**, *13*, 31.
[9] S. Fop, K. S. McCombie, E. J. Wildman, J. M. S. Skakle, J. T. S. Irvine, P. A. Connor, C. Savaniu, C. Ritter, A. C. Mclaughlin, *Nat. Mater.* **2020**, *19*, 752.
[10] J. Irvine, J. L. M. Rupp, G. Liu, X. Xu, S. Haile, X. Qian, A. Snyder, R. Freer, D. Ekren, S. Skinner, O. Celikbilek, S. Chen, S. Tao, T. H. Shin, R. O'Hayre, J. Huang, C. Duan, M. Papac, S. Li, V. Celorrio, A. Russell, B. Hayden, H. Nolan, X. Huang, G. Wang, I. Metcalfe, D. Neagu, S. G. Martín, *J. Phys. Energy* **2021**, *3*, 031502.
[11] R. A. D. Souza, A. Ramadan, S. Hörner, *Energy Environ. Sci.* **2012**, *5*, 5445.
[12] C. Korte, J. Keppner, A. Peters, N. Schichtel, H. Aydin, J. Janek, *Phys. Chem. Chem. Phys.* **2014**, *16*, 24575.
[13] B. Yildiz, *MRS Bull.* **2014**, *39*, 147.
[14] A. Fluri, D. Pergolesi, V. Roddatis, A. Wokaun, T. Lippert, *Nat. Commun.* **2016**, *7*, 10692.
[15] Y. Shi, I. Garbayo, P. Muralt, J. L. M. Rupp, *J. Mater. Chem. A* **2017**, *5*, 3900.
[16] Y. P. Ivanov, M. Kubicek, M. Siebenhofer, A. Viernstein, H. Hutter, J. Fleig, A. Chuvilin, Z. L. Zhang, *Commun. Mater.* **2020**, *1*, 1.
[17] R. Gao, A. C. P. Jain, S. Pandya, Y. Dong, Y. Yuan, H. Zhou, L. R. Dedon, V. Thoréton, S. Saremi, R. Xu, A. Luo, T. Chen, V. Gopalan, E. Ertekin, J. Kilner, T. Ishihara, N. H. Perry, D. R. Trinkle, L. W. Martin, *Adv. Mater.* **2020**, *32*, 1905178.
[18] J. Keppner, C. Korte, J. Schubert, W. Zander, M. Ziegner, D. Stolten, *Solid State Ion.* **2015**, *273*, 2.
[19] S. J. Kim, T. Akbay, J. Matsuda, A. Takagaki, T. Ishihara, *ACS Appl. Energy Mater.* **2019**, *2*, 1210.
[20] D. Neagu, G. Tsekouras, D. N. Miller, H. Ménard, J. T. S. Irvine, *Nat. Chem,* **2013**, *5*, 916.
[21] K. Kousi, C. Tang, I. S. Metcalfe, D. Neagu, *Small* **2021**, *17*, 2006479.
[22] X. Cheng, J. Sullaphen, M. Weyland, H. Liu, N. Valanoor, *APL Mater.* **2014**, *2*, 032109.
[23] G. Hautier, C. Fischer, V. Ehrlacher, A. Jain, G. Ceder, *Inorg. Chem.* **2011**, *50*, 656.
[24] A. Jain, S. P. Ong, G. Hautier, W. Chen, W. D. Richards, S. Dacek, S. Cholia, D. Gunter, D. Skinner, G. Ceder, K. A. Persson, *APL Mater.* **2013**, *1*, 011002.
[25] M. de Jong, W. Chen, T. Angsten, A. Jain, R. Notestine, A. Gamst, M. Sluiter, C. Krishna Ande, S. van der Zwaag, J. J. Plata, C. Toher, S. Curtarolo, G. Ceder, K. A. Persson, M. Asta, *Sci. Data* **2015**, *2*, 150009.
[26] T. Kushi, K. Sato, A. Unemoto, S. Hashimoto, K. Amezawa, T. Kawada, *J. Power Sources* **2011**, *196*, 7989.
[27] B. X. Huang, J. Malzbender, R. W. Steinbrech, *J. Mater. Sci.* **2011**, *46*, 4937.
[28] Y. Kimura, *Ph.D. Thesis,* Tohoku University **2015**.
[29] T. Mayeshiba, D. Morgan, *Phys. Chem. Chem. Phys.* **2014**, *17*, 2715.
[30] M. W. Ammann, J. P. Brodholt, D. P. Dobson, *Phys. Chem. Miner.* **2009**, *36*, 151.
[31] K. Syed, J. Wang, B. Yildiz, W. J. Bowman, *Nanoscale* **2022**, *14*, 663.
[32] J. Wang, K. Syed, S. Ning, I. Waluyo, A. Hunt, E. J. Crumlin, A. K. Opitz, C. A. Ross, W. J. Bowman, B. Yildiz, *Adv. Funct. Mater.* **2022**, *32*, 2108005.